

Improved Spectral Unmixing of Hyperspectral Images Using Spatially Homogeneous Endmembers

Maciel Zortea and Antonio Plaza

Department of Technology of Computers and Communications, University of Extremadura

Escuela Politecnica de Caceres, Avda. de la Universidad s/n, E-10071 Caceres, SPAIN

Contact e-mails: maciel.zortea@hyperinet.eu and aplaza@unex.es; Phone: +34 927257195; Fax: +34 927 257203

Abstract—Hyperspectral imaging is a new technique in remote sensing which provides image data at hundreds of spectral wavelengths, thus allowing a very detailed characterization of the surface of the Earth (from an airborne or satellite platform). One of the most important challenges in hyperspectral imaging is to find an adequate pool of pure signature spectra of the materials present in the scene. These pure signatures are then used to decompose the scene into a set of so-called abundance fractions by means of a spectral unmixing algorithm, thus allowing a detailed analysis of the scene with sub-pixel precision. Most techniques available in endmember extraction literature rely on exploiting the spectral properties of the data alone. As a result, the search for endmembers in a scene is often conducted by treating the data as a collection of spectral measurements with no spatial arrangement. In this paper, we propose a novel strategy to incorporate spatial information into the traditional spectral-based endmember search process. Specifically, we propose to estimate, for each pixel vector in the scene, a scalar value which is used to weight the importance of the spectral information associated to each pixel in terms of its spatial context. The proposed methodology, which favours the selection of highly representative endmembers located in spatially homogeneous areas, is shown in this work to significantly improve several spectral-based endmember extraction algorithms available in the literature. Our experimental results, obtained using real hyperspectral data collected by NASA over the Indian Pines region in Northern Indiana, are very encouraging and reveal that the proposed approach is suitable for jointly combining spectral and spatial information when searching for image-derived endmembers in highly representative hyperspectral image data sets.

Keywords—Hyperspectral signal processing, spatial-spectral analysis, endmember extraction, fractional abundance estimation, spectral unmixing.

I. INTRODUCTION

Hyperspectral imaging spectrometers such as NASA's Airborne Visible Infra-Red Imaging Spectrometer (AVIRIS) [1] provide a new class of observation data for improved Earth surface characterization, being now able to cover the wavelength region from 0.4 to 2.5 μm using more than 200 spectral channels, at nominal spectral resolution of 10 nm. Each of the pixels collected by hyperspectral imagers such as AVIRIS contains the resultant mixed spectrum from the reflected surface radiation of subpixel constituent materials within the pixel. Mixed pixels exist for several reasons. First, if the spatial resolution of the sensor is not high enough to separate different pure signature materials at a macroscopic level, these can jointly occupy a single pixel, and the resulting spectral measurement will be a composite of the individual spectra. Second, mixed pixels can also result when distinct materials are combined into a homogeneous mixture. This

circumstance also occurs independent of the spatial resolution of the sensor. To deal with this problem, linear spectral mixture analysis techniques first identify a collection of spectrally pure constituent spectra, often called *endmembers* in the literature, and then express the measured spectrum of each mixed pixel as a linear combination of endmembers weighted by fractions or abundances that indicate the proportion of each endmember present in the pixel [2].

Over the last decade, several algorithms have been developed for automatic or semi-automatic extraction of spectral endmembers directly from an input hyperspectral data set. Some classic techniques for this purpose include the pixel purity index (PPI) [3], N-FINDR [4], iterative error analysis (IEA) [5], optical real-time adaptive spectral identification system (ORASIS) [6], convex cone analysis (CCA) [7], and an orthogonal subspace projection (OSP) technique in [8]. Other advanced techniques for endmember extraction have been recently proposed [9], [10], [11], [12], [13], [14], [15], [16], being most of them focused on analyzing the data without incorporating information on the spatially adjacent data, i.e., the hyperspectral data is not really treated as an image but as an unordered listing of spectral measurements with no spatial arrangement. However, one of the distinguishing properties of hyperspectral data is the multivariate information coupled with a two-dimensional (pictorial) representation amenable to image interpretation.

A possible approach to take advantage of spatial information when searching for image endmembers is to exploit the spatial similarity between adjacent pixels by defining a criterion which is sensitive to the nature of both *homogenous* and *transition* areas between different land-cover classes. Intuitively, the transition areas between two or more different land-cover types would likely contain some mixed pixels. Conversely, by definition, an endmember is an idealized pure signature for a class. Thus, it would be reasonable to assume that pure pixels are less likely to be found in such transition areas. In other words, if homogenous areas can be generally expected to provide best candidate pixel vectors for endmember extraction algorithms, then it is also possible to use the spatial information to intelligently direct the spectral-based endmember search process to these spatially homogeneous and highly representative regions.

With the above ideas in mind, this work develops a novel framework for the integration of spatial and spectral informa-

tion in the process of endmember extraction. The proposed approach is presented as a preprocessing module which can be used in combination with available endmember extraction algorithms. The method takes advantage of a particular characteristic of remotely sensed scenes, in which spatially adjacent pixel vectors are expected to share similar information, from a spectral point of view. To exploit this feature, our approach relies on the introduction of a spatial-based pixel similarity measure which is used to weight the spectral signature associated to each pixel vector according to its spatial context.

The remainder of the paper is organized as follows. Section II formulates and describes the proposed preprocessing method, including a geometric interpretation. Section III briefly reviews three spectral-based endmember extraction algorithms that will be used in this work in conjunction with the proposed preprocessing module to substantiate its advantages, and then describes the hyperspectral data set used for evaluation purposes. Experimental results analyzing the performance of the considered endmember extraction algorithms with and without the proposed preprocessing method are discussed in Section IV. Finally, section V concludes with some remarks and hints at plausible future research.

II. METHODOLOGY

A. Problem Formulation

Let us assume that a remotely sensed hyperspectral scene with n bands is denoted by \mathbf{I} , in which the pixel at the discrete spatial coordinates (i, j) of the scene is represented by a vector $\mathbf{X}(i, j) = [x_1(i, j), x_2(i, j), \dots, x_n(i, j)] \in \mathfrak{R}^n$, where \mathfrak{R} denotes the set of real numbers in which the pixel's spectral response $x_k(i, j)$ at sensor channels $k = 1, \dots, n$ is included. Under the linear mixture model assumption, each pixel vector in the original scene can be modeled using the following expression:

$$\mathbf{X}(i, j) = \sum_{z=1}^p \Phi_z(i, j) \cdot \mathbf{E}_z + \mathbf{n}(i, j), \quad (1)$$

where \mathbf{E}_z denotes the spectral response of endmember z , $\Phi_z(i, j)$ is a scalar value designating the fractional abundance of the endmember z at the pixel $\mathbf{X}(i, j)$, p is the total number of endmembers, and $\mathbf{n}(i, j)$ is a noise vector. The solution of the linear spectral mixture problem described in (1) relies on a successful estimation of how many endmembers, p , are present in the input hyperspectral scene \mathbf{I} , and also on the correct determination of a set $\{\mathbf{E}_z\}_{z=1}^p$ of endmembers and their correspondent abundance fractions $\{\Phi_z(i, j)\}_{z=1}^p$ at each pixel $\mathbf{X}(i, j)$. Two physical constraints are generally imposed into the model described in (1), these are the abundance non-negativity constraint (ANC), i.e., $\Phi_z(i, j) \geq 0$, and the abundance sum-to-one constraint (ASC), i.e., $\sum_{z=1}^p \Phi_z(i, j) = 1$. In this case, we refer to the mixture model as fully constrained linear spectral unmixing (FCLSU) [17].

In addition, we assume that the input data set \mathbf{I} contains at least one pure pixel for each distinct material present in the scene, and therefore a search procedure aimed at finding the most spectrally pure signatures in the input scene is feasible. In this case, the final set of image-derived endmembers is denoted by $\Omega = (\mathbf{E}_1, \dots, \mathbf{E}_p) \subset \mathbf{I}$.

In order to incorporate the spatial information into the process of automatically selecting spectral endmembers, we estimate, for each input pixel vector, a scalar factor $\rho(i, j)$ which is intimately related to the spatial similarity between the pixel and its spatial neighbors, and then use this scalar factor to spatially weight the spectral information associated to the pixel. In order to define this procedure in mathematical terms, let us first consider a square-shaped spatial region of $ws \times ws$ pixels in size, centered at the pixel $\mathbf{X}(i, j)$. In this case, we assume that 1) ws is an odd number, and 2) the processing window has a radius of $d = (ws - 1)/2$ pixels. These values define the neighborhood region that will be considered around each pixel under analysis. With the above assumptions in mind, we can define a scalar weight $\alpha(i, j)$ as follows:

$$\alpha(i, j) = \sum_{r=i-d}^{i+d} \sum_{s=j-d}^{j+d} \beta(r-i, s-j) \cdot \gamma(r-i, s-j), \quad (2)$$

with:

$$\gamma(r-i, s-j) = \gamma(\mathbf{X}(r, s), \mathbf{X}(i, j)), \quad (3)$$

where γ refers to a similarity measure calculated between the central pixel $\mathbf{X}(i, j)$ and a neighboring pixel $\mathbf{X}(r, s)$. The value resulting from this measure is weighted by β , a scalar value that allows us to assign a different weight to the values of γ calculated inside the region delimited by the window with size $ws \times ws$ pixels. In particular, this approach allows us to give more importance to pixels which are spatially adjacent to the central pixel in the window, thus reducing the weight associated to the values of γ calculated for pixels which are more distant, spatially, from such central pixel.

With the previous rationale in mind, we define a per-pixel, spatially-derived weighting factor for endmember extraction by the following quadratic expression:

$$\rho(i, j) = \left(1 + \sqrt{\alpha(i, j)}\right)^2. \quad (4)$$

The expression above can be simply used to scale the spectral response of an original image pixel as follows:

$$\mathbf{X}(i, j)' = \frac{1}{\rho(i, j)} (\mathbf{X}(i, j) - \bar{\mathbf{I}}) + \bar{\mathbf{I}}, \quad (5)$$

where the term $\mathbf{X}(i, j)'$ denotes a spectral signature obtained after weighting $\mathbf{X}(i, j)$ using spatial information, and $\bar{\mathbf{I}}$ is the centroid of the data cloud, computed as the mean of all the pixel vectors in the original hyperspectral scene \mathbf{I} .

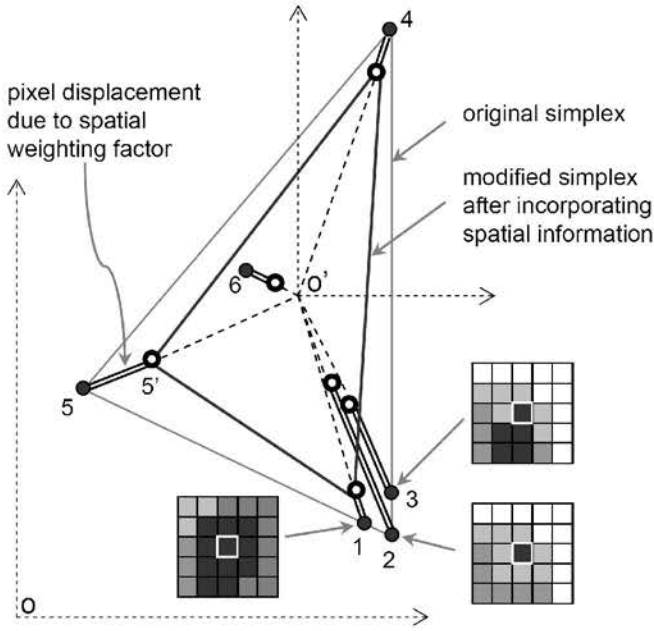


Fig. 1. Geometric interpretation of the proposed preprocessing framework.

B. Geometric Interpretation

A simple geometric interpretation of the weighting factor described in Eq. (5) is illustrated in Fig. 1, given as a toy example in which only two spectral bands of an input hyperspectral scene are represented against each other for visualization purposes. As shown by Fig. 1, the idea behind our preprocessing framework is to center each spectral feature in the data cloud around its mean value, and then shift each feature straight towards the centroid of the data cloud (denoted by O' in Fig. 1) using a spatial-spectral factor given by Eq. (4). The shift of each spectral feature in the data cloud is proportional to a similarity measure calculated using both the spatial neighborhood around the pixel under consideration and the spectral information associated to the pixel, but without averaging the spectral signature of the pixel. The correction is performed so that pixels located in spatially homogenous areas (such as the pixel vector labeled as '1' in Fig. 1) are expected to have a smaller displacement with regards to their original location in the data cloud than pure pixels surrounded by spectrally distinct substances (e.g., the pixel vector labeled as '3' in Fig. 1). Resulting from the above operation, a modified simplex is formed, using not only spectral but also spatial information. It should be noted that the vertices of the modified simplex are more likely to be pure pixels located in spatially homogenous areas. Although the proposed method is expected to privilege homogeneous areas for the selection of endmembers, no pixel is excluded from the competitive endmember extraction process that follows the preprocessing. As it can be inferred from Fig. 1, the proposed method is also expected to be robust in the presence of outliers.

It is important to notice that the modified simplex in Fig. 1 is mainly intended to serve as a guide for a subsequent competitive endmember extraction process, conducted using a user-defined algorithm. However, such modified simplex is not intended to replace the simplex in the input hyperspectral scene. To achieve this, the spatial coordinates of the endmembers extracted from the preprocessed image are retained, but the spectral signatures associated to those spatial coordinates are obtained from the original hyperspectral scene as depicted in Fig. 2, which provides a flowchart of the preprocessing technique in combination with a certain endmember extraction and spectral unmixing algorithm. As shown by Fig. 2, the estimation of the number of endmembers is conducted using the original hyperspectral image as input. On the other hand, the modified hyperspectral image resulting from our spatial preprocessing is only used as input to the endmember extraction algorithm. The spatial coordinates of extracted endmembers are retained and used to form a final set Ω which comprises the original image pixels at such coordinates. Then, a spectral unmixing process is conducted using the original hyperspectral image and the set Ω as inputs. As a result, no artifacts are introduced in the process of estimating abundance fractions.

To conclude this subsection, we emphasize that the general flowchart described in Fig. 2 can be used in combination with different techniques for endmember extraction and spectral unmixing. Also, the factor described in Eq. (4) can be defined using different measures for the spectral similarity criterion γ and the spatial weight function β defined in Eq. (2). In the following subsection, we describe our empirical choices for both parameters in this work.

C. Spectral Similarity Metric and Spatial Neighborhood Weight

Several point-wise distances can be considered in order to compute the spectral similarity measure γ used in Eq. 4. In this work, we have used the spectral angle distance (SAD), a well known measure for hyperspectral data processing [18]. SAD can be used to measure the spectral similarity between two pixel vectors, $\mathbf{X}(i, j)$ and $\mathbf{X}(r, s)$, as follows:

$$\gamma = \text{SAD}(\mathbf{X}(i, j), \mathbf{X}(r, s)) = \cos^{-1} \frac{\mathbf{X}(i, j) \cdot \mathbf{X}(r, s)}{\|\mathbf{X}(i, j)\| \|\mathbf{X}(r, s)\|}. \quad (6)$$

It should be noted that SAD is given by the cosine of the spectral angle formed by n -dimensional vectors. As a result, this measure is invariant in the multiplication of $\mathbf{X}(i, j)$ and $\mathbf{X}(r, s)$ by constants and, consequently, is invariant before unknown multiplicative scalings that may arise due to differences in illumination and angular orientation [19].

On the other hand, the spatial weight function $\beta(i, j)$ is taken as the quadratic distance of each pixel inside the region ws and the central pixel, normalized by a constant ζ :

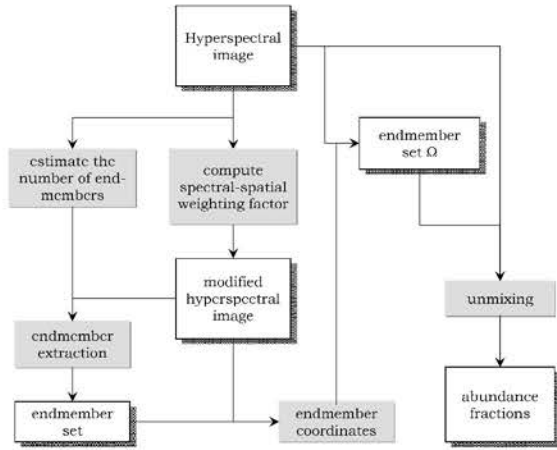


Fig. 2. Flowchart of the proposed method for incorporating spatial-spectral information into the endmember extraction and unmixing process.

$$\beta(i, j) = \begin{cases} 0, & \text{if } i = 0 \text{ and } j = 0; \\ \frac{1}{\zeta(i^2 + j^2)}, & \text{otherwise,} \end{cases} \quad (7)$$

where:

$$\zeta = \sum_{r=i-d}^{i+d} \sum_{s=j-d}^{j+d} \frac{1}{[(r-i)^2 + (s-j)^2]}, \text{ for } (r, s) \neq (i, j). \quad (8)$$

Thus, the SAD spectral similarity score obtained after comparing the spectral signature associated to the central pixel with that of its spatial neighbors receives more importance than the scores obtained after comparing the same pixel with more distant neighbors. It should be noted that the constant ζ in Eq. (7) is not strictly necessary, but it allows one to control the importance of the similarity score obtained after comparing two pixel vectors into the interval $0 \leq \beta(i, j) < 1$.

III. EXPERIMENTAL SET-UP

A. Endmember Extraction Algorithms

Three well-known endmember extraction algorithms have been selected for our comparative study, including the N-FINDR algorithm in [4], the VCA algorithm in [20], and the OSP algorithm in [8]. The reason for our selection is that these three algorithms are representative of a class of convex geometry-based techniques which have been quite successful in the task of endmember extraction, and which are also fully automatic in nature. In our experiments with VCA, we select the corresponding pixel original spectra as the VCA solution, not the noise-smoothed solution produced by the original algorithm.

It should be noted that, in our experimental assessment, the three above-mentioned algorithms will be applied to a transformed data set obtained after applying our preprocessing framework to the original hyperspectral image. However, the final endmember set is not obtained from the transformed image but from the original one, after retaining the spatial

coordinates of the endmembers found in the transformed data set.

B. AVIRIS Indian Pines Scene

This scene, with a size of 145×145 pixels, was acquired by the AVIRIS sensor in June 1992 over the Indian Pines area in Northwestern Indiana, a mixed agricultural/forest area, early in the growing season. The scene comprises 220 spectral channels in the wavelength range $0.4\text{--}2.5 \mu\text{m}$. After an initial screening, several noisy spectral bands were removed from the data set, leaving a total of 190 radiance channels to be used in the experiments. For illustrative purposes, Fig. 3(a) shows a false color composition of the AVIRIS Indian Pines scene, while Fig. 3(b) shows the ground-truth map available for the scene, displayed in the form of a class assignment for each labeled pixel, presents 16 mutually exclusive ground-truth classes. These data, including ground-truth, are available online¹, a fact which has made this scene a widely used benchmark for testing the accuracy of hyperspectral data classification algorithms. Unfortunately, no ground-truth information about the location of pure pixels and/or the true fractional abundances of endmembers is available for this scene (as it is often the case in most real-world applications). Despite the lack of ground truth at sub-pixel levels, an alternative strategy will be used in this work to validate the quality of extracted endmembers using available labeled pixels.

IV. COMPARATIVE PERFORMANCE ANALYSIS

Our analysis with this real hyperspectral scene begins with the estimation of the number of endmembers p present in the scene, using the virtual dimensionality (VD) concept in [21]. A reasonable estimate for the VD seemed to be 18. The value of $p = 18$ also seems reasonable in light of the number of distinct land-cover classes labeled in the ground-truth map. Therefore, only the experiments for a case study with $p = 18$ are discussed in this subsection.

The analysis presented in this section has been conducted under the assumption that, as it is often the case with real hyperspectral scenes, there is no ground-truth information about the location of pure pixels or their true abundance fractions at a pixel-level in the scene. In this case, the only available information *a priori* is a ground-truth map which assigns a (hard) class label to each image pixel, with no further information about sub-pixel abundance fractions. In this context, our hypothesis is that a set of high-quality endmembers (and their corresponding FCLSU-estimated abundance fractions) may allow reconstruction of the original hyperspectral scene [by means of Eq. (1)] with highest precision than a set of low-quality endmembers. In other words, our main goal in experiments with this scene is to analyze the reconstruction error, which can be seen as an indirect assessment of the accuracy of both the endmember extraction and the linear spectral unmixing stages. It should be noted that the same FCLSU

¹<http://dynamo.ecn.purdue.edu/biehl/MultiSpec>



Fig. 3. (a) False color composition of the AVIRIS Indian Pines scene. (b) Ground truth-map containing 16 mutually exclusive land-cover classes (right).

unmixing algorithm is always used to estimate the fractional abundances of different sets of endmembers produced by different algorithms with and without spatial preprocessing, thus allowing us to individually substantiate the impact of spatial preprocessing.

The measure employed to evaluate the goodness of the reconstruction is the root mean square error (RMSE) between the original and the reconstructed hyperspectral scene, which can be defined as follows. Let us assume that $\mathbf{I}^{(O)}$ is the original hyperspectral scene, and that $\mathbf{I}^{(R)}$ is a reconstructed version of $\mathbf{I}^{(O)}$, obtained using Eq. (1) with a set of endmembers, automatically derived by a certain algorithm from the original scene, and their corresponding FCLSU-estimated fractional abundances. Let us also assume that the pixel vector at spatial coordinates (i, j) in the original hyperspectral scene is given by $\mathbf{X}^{(O)}(i, j) = [x_1^{(O)}(i, j), x_2^{(O)}(i, j), \dots, x_n^{(O)}(i, j)]$, while the corresponding pixel vector at the same spatial coordinates in the reconstructed hyperspectral scene is given by $\mathbf{X}^{(R)}(i, j) = [x_1^{(R)}(i, j), x_2^{(R)}(i, j), \dots, x_n^{(R)}(i, j)]$. With the above notation in mind, the RMSE between the original and the reconstructed hyperspectral scenes is calculated as follows:

$$\text{RMSE}(\mathbf{I}^{(O)}, \mathbf{I}^{(R)}) = \frac{1}{s \times l} \sum_{i=1}^s \sum_{j=1}^l \left(\frac{1}{n} \sum_{k=1}^n [x_k^{(O)}(i, j) - x_k^{(R)}(i, j)]^2 \right)^{\frac{1}{2}}. \quad (9)$$

Table 1 reports the overall RMSE scores calculated using the expression in Eq. (9) and also the individual, per-class RMSE scores calculated using only the spatial coordinates of the pixels labeled as belonging to a certain land-cover class in the ground-truth map available for the AVIRIS Indian Pines scene. In each reconstruction, we used the endmembers produced by three different extraction algorithms (OSP, N-FINDR and VCA) with no spatial preprocessing ($ws = 0$) and with spatial preprocessing, using window sizes of $ws = 3$, $ws = 5$ and $ws = 9$, respectively. From Table 1, it can be observed that spatial preprocessing allows a significant reduction of both the overall and individual RMSE scores. This is particularly the case for land-cover classes made up of homogeneous pixels (e.g., *Corn*, *Grass* and *Soybeans*), while

the land-cover classes mainly formed by anomalous pixels (e.g., the *Bldg-Grass-Trees* class) exhibit a less significant reduction of individual RMSE scores. Finally, Table 1 also reveals that the overall RMSE error after comparing the original scene with a reconstructed version using endmembers produced after spatial preprocessing was always lower than the RMSE error after comparing the original scene with a reconstructed version using endmembers directly extracted from the original hyperspectral scene, with $ws = 5$ apparently providing a good compromise for the window size as indicated by results in the table.

V. CONCLUDING REMARKS

The main contribution of this paper is the development of a simple, yet effective methodology which integrates both the spatial and the spectral information contained in the hyperspectral data in simultaneous fashion. The proposed methodology allows one to incorporate spatial information into the traditional spectral-based endmember search conducted by standard algorithms, with the peculiarity that the algorithms used for endmember searching do not need to be modified. Instead, the proposed approach works as an (optional) spatial preprocessing module which can be applied to the original hyperspectral image prior to the execution of an endmember extraction algorithm, thus allowing one to make use of the standard hyperspectral processing chain for spectral unmixing since this module works independently of other relevant modules of such chain, such as dimensionality reduction, endmember extraction or spectral unmixing.

Our experiments using real hyperspectral data sets revealed that the proposed approach is quite promising in the sense that it can take advantage of spatial information in order to intelligently guide the traditional, spectral-based approach to extract endmembers from a hyperspectral scene, and also avoid that important endmembers are discarded during the process. Despite the above remarks, further experimentation should be conducted in future work to address some unresolved issues that may present challenges over time. Specifically, an evaluation of different distance measures to be used in the

Table 1. Individual and overall RMSE-based reconstruction errors obtained after comparing the original AVIRIS Indian Pines scene with a reconstructed version of the same scene using the fully constrained linear mixture model in Eq. (1) and the endmembers extracted by OSP, N-FINDR and VCA algorithms. Two cases are reported for each algorithm: no spatial preprocessing ($ws = 0$), and spatial preprocessing prior to endmember extraction, using window sizes of $ws = 3$, $ws = 5$ and $ws = 9$.

Class (number of pixels)	OSP				N-FINDR				VCA			
	$ws = 0$	$ws = 3$	$ws = 5$	$ws = 9$	$ws = 0$	$ws = 3$	$ws = 5$	$ws = 9$	$ws = 0$	$ws = 3$	$ws = 5$	$ws = 9$
Alfalfa (54)	55.16	45.90	44.99	47.28	33.16	41.53	41.98	37.77	70.18	49.12	37.84	46.34
Corn-notill (1434)	37.76	23.49	25.18	33.89	40.17	26.40	31.85	30.01	35.48	30.49	33.06	31.31
Corn-min (834)	32.44	25.03	26.55	31.04	36.11	28.29	28.90	28.28	33.86	28.11	32.10	29.68
Corn (234)	36.22	26.48	26.79	42.86	43.19	28.56	38.47	29.12	38.81	33.46	34.74	34.67
Grass/Pasture (497)	41.08	34.93	27.50	32.23	106.71	37.52	30.11	28.91	45.41	27.17	27.69	57.66
Grass/Trees (747)	30.32	27.23	24.12	36.52	31.42	25.12	30.05	26.46	26.41	23.51	23.25	28.72
Grass/pasture-mowed (26)	32.74	26.06	26.33	26.96	23.93	24.31	26.27	22.78	38.68	33.97	24.24	25.76
Hay-windrowed (489)	59.46	35.72	34.06	46.81	35.59	31.08	39.72	29.94	65.39	57.00	33.04	34.87
Oats (20)	26.04	25.73	23.27	25.53	25.33	25.65	24.72	23.14	25.39	25.31	23.68	24.22
Soybeans-notill (968)	47.07	22.55	24.11	31.58	51.32	26.72	33.60	31.02	27.59	24.49	26.37	25.01
Soybeans-min (2468)	46.08	24.93	27.10	33.71	48.28	31.98	34.01	31.93	36.13	28.93	33.45	31.14
Soybeans-clean (614)	45.09	23.89	24.52	49.26	54.35	25.31	44.59	29.82	31.76	26.97	26.96	25.85
Wheat (212)	29.58	31.16	26.77	29.20	27.18	25.81	26.36	33.12	26.99	26.19	29.65	27.36
Woods (1294)	50.21	51.99	27.81	27.86	91.95	47.18	36.88	38.05	40.84	37.01	42.88	49.38
Bldg-Grass-Trees (380)	43.97	45.95	30.04	33.32	34.73	39.05	32.49	35.61	33.09	33.02	35.73	35.98
Stone-steel towers (95)	93.62	70.79	49.52	61.11	98.25	36.43	36.12	105.28	92.80	36.84	56.67	45.32
Overall RMSE-based error	40.80	34.24	27.37	32.97	47.49	32.93	32.48	32.48	35.60	30.62	32.19	34.23

extension of the proposed preprocessing framework is a key topic deserving future research. In addition, tests with alternative spatial-weighting formulations should also be conducted. Finally, parallel implementations of the proposed methodology are currently being developed in our laboratory for speeding up its computational performance.

ACKNOWLEDGMENTS

This work has been supported by the European Community's Marie Curie Research Training Networks Programme under contract MRTN-CT-2006-035927, Hyperspectral Imaging Network (HYPER-I-NET). The authors gratefully acknowledge Dr. David A. Landgrebe for providing the hyperspectral data set used in experiments. Dr. Jose Bioucas-Dias and Dr. Jose Nascimento are also gratefully acknowledged for providing an implementation of VCA algorithm.

REFERENCES

- [1] R. O. Green, M. L. Eastwood, C. M. Sarture, T. G. Chrien, M. Aronsson, B. J. Chippendale, J. A. Faust, B. E. Pavri, C. J. Chovit, M. Solis, et al., "Imaging spectroscopy and the airborne visible/infrared imaging spectrometer (AVIRIS)," *Remote Sensing of Environment*, vol. 65, no. 3, pp. 227–248, 1998.
- [2] J. B. Adams, M. O. Smith, and P. E. Johnson, "Spectral mixture modeling: a new analysis of rock and soil types at the Viking Lander 1 site," *Journal of Geophysical Research*, vol. 91, pp. 8098–8112, 1986.
- [3] J. W. Boardman, F. A. Kruse, and R. O. Green, "Mapping Target Signatures Via Partial Unmixing of Aviris Data," *Proc. JPL Airborne Earth Sci. Workshop*, pp. 23–26, 1995.
- [4] M. E. Winter, "N-FINDR: an algorithm for fast autonomous spectral end-member determination in hyperspectral data," *Proc. SPIE Image Spectrometry V*, vol. 3753, pp. 266–277, 2003.
- [5] R. A. Neville, K. Staenz, T. Szeredi, J. Lefebvre, and P. Hauff, "Automatic endmember extraction from hyperspectral data for mineral exploration," *Proc. 21st Canadian Symp. Remote Sens.*, pp. 21–24, 1999.
- [6] J. H. Bowles, P. J. Palmadesso, J. A. Antoniadis, M. M. Baumbach, and L. J. Rickard, "Use of filter vectors in hyperspectral data analysis," *Proc. SPIE Infrared Spaceborne Remote Sensing III*, vol. 2553, pp. 148–157, 1995.
- [7] A. Ifarraguerri and C.-I. Chang, "Multispectral and hyperspectral image analysis with convex cones," *IEEE Transactions on Geoscience and Remote Sensing*, vol. 37, no. 2, pp. 756–770, 1999.
- [8] H. Ren and C.-I. Chang, "Automatic spectral target recognition in hyperspectral imagery," *IEEE Transactions on Aerospace and Electronic Systems*, vol. 39, no. 4, pp. 1232–1249, 2003.
- [9] M. Berman, H. Kivveri, R. Lagerstrom, A. Ernst, R. Dunne, and J. F. Huntington, "ICE: a statistical approach to identifying endmembers in hyperspectral images," *IEEE Transactions on Geoscience and Remote Sensing*, vol. 42, no. 10, pp. 2085–2095, 2004.
- [10] D. M. Rogge, B. Rivard, J. Zhang, and J. Feng, "Iterative spectral unmixing for optimizing per-pixel endmember sets," *IEEE Transactions on Geoscience and Remote Sensing*, vol. 44, no. 12, pp. 3725–3736, 2006.
- [11] L. Miao and H. Qi, "Endmember extraction from highly mixed data using minimum volume constrained nonnegative matrix factorization," *IEEE Transactions on Geoscience and Remote Sensing*, vol. 45, no. 3, pp. 765–777, 2007.
- [12] C.-I. Chang, C.-C. Wu, W. Liu, and Y.-C. Ouyang, "A new growing method for simplex-based endmember extraction algorithm," *IEEE Transactions on Geoscience and Remote Sensing*, vol. 44, no. 10, pp. 2804–2819, 2006.
- [13] J. Wang and C.-I. Chang, "Applications of independent component analysis in endmember extraction and abundance quantification for hyperspectral imagery," *IEEE Transactions on Geoscience and Remote Sensing*, vol. 44, no. 9, pp. 2601–2616, 2006.
- [14] A. Plaza and C.-I. Chang, "Impact of initialization on design of endmember extraction algorithms," *IEEE Transactions on Geoscience and Remote Sensing*, vol. 44, no. 11, pp. 3397–3407, 2006.
- [15] C.-I. Chang and A. Plaza, "A fast iterative algorithm for implementation of pixel purity index," *IEEE Geoscience and Remote Sensing Letters*, vol. 3, no. 1, pp. 63–67, 2006.
- [16] A. Zare and P. Gader, "Hyperspectral band selection and endmember detection using sparsity promoting priors," *IEEE Geoscience and Remote Sensing Letters*, vol. 5, no. 2, pp. 256–260, 2008.
- [17] D. Heinz and C.-I. Chang, "Fully constrained least squares linear mixture analysis for material quantification in hyperspectral imagery," *IEEE Trans. Geosci. Remote Sensing*, vol. 39, no. 3, 2001.
- [18] C.-I. Chang, *Hyperspectral Imaging: Techniques for Spectral Detection and Classification*. Kluwer Academic/Plenum Publishers: New York, 2003.
- [19] N. Keshava and J. F. Mustard, "Spectral unmixing," *IEEE Signal Processing Magazine*, vol. 19, no. 1, pp. 44–57, 2002.
- [20] J. M. P. Nascimento and J. M. Bioucas-Dias, "Vertex Component Analysis: A Fast Algorithm to Unmix Hyperspectral Data," *IEEE Transactions on Geoscience and Remote Sensing*, vol. 43, no. 4, pp. 898–910, 2005.
- [21] C.-I. Chang and Q. Du, "Estimation of number of spectrally distinct signal sources in hyperspectral imagery," *Geoscience and Remote Sensing, IEEE Transactions on*, vol. 42, no. 3, pp. 608–619, 2004.